



The resonant acoustic signatures of lithic debitage

Margaret A. Morris ^{a,*}, Petr Krysl ^b, Isabel C. Rivera-Collazo ^{a,c}, John A. Hildebrand ^a

^a Scripps Institution of Oceanography, University of California, San Diego, 9500 Gilman Drive MC:0205 La Jolla, CA 92093-0205, United States

^b Department of Structural Engineering, University of California, San Diego, 9500 Gilman Drive MC:0085 La Jolla, CA 92093-0085, United States

^c Department of Anthropology, University of California, San Diego, 9500 Gilman Drive MC:0218 La Jolla, CA 92093-0218, United States



ARTICLE INFO

Keywords:

Underwater archaeology
Lithics
Sonar
Acoustic detection
Finite elements
Boundary element method

ABSTRACT

Acoustic methods to search for submerged archaeological sites have shown that concentrations of knapped flint produce a visible acoustic response in chirp sonar profiles in a variety of geographical settings. Field tests and simulations have suggested that the submerged lithic signal is due to acoustic resonances of the flaked stone. We model and measure the resonant acoustic signatures of chert, obsidian, metavolcanic, and granitic lithic debitage. Struck lithics produce multiple resonant peaks under 30 kHz, with high quality factors that decrease with material coarseness. We use a combination of the finite element and boundary element methods to model the natural vibrations of lithic debitage in both air and water. Direct measurement of lithic material density and adjustment of the Young's modulus and Poisson's ratio provide excellent correspondence between measured and modeled resonances. Using a coupled finite element and boundary integral method, we model the acoustic scattering return of individual lithics in water as a function of frequency and incidence angle. We find the strongest resonant signal between 8 and 16 kHz for a collection of lithic debitage. Results indicate that the lithic resonance signal is highly directional, with target strength up to -20 dB when excited at optimal angles. For a flat-laying lithic, target strength at normal incidence is, on average, 10 dB lower than the strongest signal, typically found $55^\circ \pm 18^\circ$ from normal incidence. We suggest that the best way to detect submerged lithics may not be through standard mono-static sub-bottom profiling with a direct downward pulse, but with a chirp pulse sent and received at an angle with respect to the sea bottom.

1. Introduction

Coastal lands that were inundated since the last glacial maximum hold key information about human migration, trade, land use, and climate change adaptations (Bailey and King, 2011; Bailey and Flemming, 2008; Braje et al., 2019; Erlandson, 2001). Advances in paleo-landscape reconstruction and modeled site prediction have demonstrated that archaeological information can be preserved in submerged sites (Benjamin, 2010; Watts et al., 2011; Westley et al., 2011; Flemming et al., 2017; McLaren et al., 2020); however, relatively few submerged sites have been directly detected (Sturt et al., 2018). Site detection is necessary to test site occurrence prediction models and generate new data in the form of cultural materials and associated landscape characteristics.

The predominant means of submerged site detection are through diver surveys and chance finds, with chance accounting for the majority of reported sites (Flemming, 2020). Divers are only able to see what is visible on the seafloor, so entirely buried sites are missed. Chance finds

are unreliable, and many occur through destructive means, such as dredging and trawling, which alter the underwater landscape and remove artifacts from their associated context. Other chance finds are costly and inconvenient, as offshore development projects can be delayed by an accidental site discovery. With international emphasis on developing a blue economy (European Commission, 2020), in which marine resources are optimally exploited while still being preserved, it becomes increasingly important to develop reliable, non-destructive methods for site detection and study. While offshore developments plan and budget for mitigation needs, revealing archaeological material early in the planning process would add time to re-think project proposals to avoid large scale impact and reduce the need for costly mitigation. Further, the importance of underwater cultural heritage is formally recognized in the UNESCO 2001 convention (UNESCO, 2001), which promotes *in situ* preservation of underwater sites. The goal is to avoid impact, rather than settle for mitigation after impact occurs. Effective remote-sensing methods would prevent costly delays to development projects in marine environments, decrease destruction of

* Corresponding author.

E-mail address: mam132@ucsd.edu (M.A. Morris).

benthic habitats, and preserve underwater archaeological information *in situ*, satisfying multiple internationally recognized objectives.

A primary difficulty in detecting prehistoric sites is that objects left behind are often buried and too small to be readily detected by standard marine survey methods (Flemming et al., 2014; Plets et al., 2013; Astrup et al., 2019; McCarthy et al., 2019). Ole Grøn and colleagues (Grøn et al., 2021; Grøn et al., 2017) propose a sub-bottom acoustic profiling method to search specifically for knapped stone, which is a clear indicator of human presence and is widely ubiquitous in prehistoric archaeological sites. The proposed method has already facilitated submerged site discovery in varied geographical settings, with concentrations of knapped stone producing a visible acoustic response in minimally processed chirp sub-bottom profiles. They suggest that the method's success is due to the lithics' strong resonance properties, which have been demonstrated in both experiments (Blake and Cross, 2008; Grøn et al., 2018, 2021) and preliminary models (Hermand et al., 2011; Hermand and Tayong, 2013).

While this method has led to site discoveries, its potential is just beginning to be understood. The method recommends looking for a diffuse 'haystack' signal in the water column portion of sub-bottom profiles. Why the signal appears in the water column remains a mystery, since the lithics are located within the sediment. As it stands, the signal cannot be used to infer the depth and extent of buried lithics, nor any properties of the lithics themselves; however, the success of the method gives confidence that acoustic remote sensing can provide such information. To retrieve this data, it is necessary to (1) learn more about lithics' acoustic properties and (2) use more advanced data processing methods to detect and interpret the lithic signatures. This paper begins to address the first of these necessities, which is a prerequisite to the second.

We present the modeled and measured acoustic response of an assortment of lithic debitage. The lithics' acoustic resonance frequencies are modeled in both air and water using a combined finite element and boundary element method and tested against measured data for object resonance in air. We characterize strength and directionality of the acoustic response of flat-laying lithics by simulating the acoustic return of individual lithics insonified by a plane wave using a coupled finite element and boundary integral method (Abawi, 2017; Abawi and Krysl, 2017). We explore relationships between lithic properties (material and dimensional) and resonance frequencies using a thin-plate vibration approximation. By understanding what frequency range and signal strength to expect for different types of lithics, we can use expected lithic types to help guide sonar searches for sites. Directionality in the acoustic response is presented, and results are used to suggest modifications to currently proposed detection methods.

2. Materials & methods

2.1. Lithic assortment

2.1.1. Source and material properties

We analyzed 40 specimens of lithic debitage, comprised of 37 pieces knapped by G. Timothy Gross (pers. comm.), and 3 granitic artifacts from the archaeological site of Angostura in Barceloneta, Puerto Rico (obtained by I. C. Rivera-Collazo). Four lithic materials were chosen to represent a range of knapping material: glass - obsidian ($n = 9$), cryptocrystalline - pink chert ($n = 19$), fine-grained crystalline - Santiago Peak metavolcanic rock ($n = 9$), and coarser-grained crystalline - granitic rock ($n = 3$). The lithic materials were characterized in the model by their density, ρ , Young's modulus, E , and Poisson's ratio, ν . Density was measured by a water-displacement buoyancy method employing Archimedes' principle. Young's modulus and Poisson's ratio were chosen to match modeled resonant frequencies (Section 2.3) with measured lithic spectrum peaks (Section 2.2) for a subset of the examples for each material. Initial values of E_0, ν_0 chosen from literature (obsidian: $E_0 = 70$ GPa, $\nu_0 = 0.08$ (Klein and Carmichael, 2021), chert:

$E_0 = 80$ GPa, $\nu_0 = 0.125$ (Aliyu et al., 2017), metavolcanic: $E_0 = 88$ GPa, $\nu_0 = 0.2$ (Lógo and Vásárhelyi, 2019), granitic: $E_0 = 50$ GPa, $\nu_0 = 0.2$ (Klein and Carmichael, 2021)) were used to model resonant frequencies in air. E was fit to the first and second resonant frequencies of a selection of lithics, using $E = E_0 \times (f_{\text{measured}}/f_{\text{modeled}})^2$. To determine ν , we modeled the air resonant frequencies, using the new E , for $\nu = 0.6\nu_0, 0.8\nu_0, \nu_0, 1.2\nu_0, 1.4\nu_0$, and chose ν to minimize error between the measured and modeled frequencies below 20 kHz. Chosen values are shown in Table 1, and are consistent with those in existing literature.

2.1.2. Digital reconstruction of lithics

Digital reconstructions of lithics were created by photogrammetry, using the software *Agisoft Metashape Standard*. The mesh generated by metashape was scaled and coarsened in *Autodesk Fusion 360*. Mesh size was chosen to balance the trade-off between model accuracy and computation time, keeping modeled resonances within 5% of those measured in air for frequencies up to 50 kHz. A tetrahedral mesh in the *Abaqus* file format was generated using *gmsh* for input into the acoustic models.

2.2. Recorded resonance

The resonant frequencies of a selection of lithics were excited in air through direct percussion. Individual lithics rested atop a rubber band, allowing them to vibrate freely. Each lithic was struck by small metal spheres (BBs) about 20 times successively, with enough time between impacts for the lithic vibration to cease. The lithic was re-positioned multiple times to ensure that all resonant frequencies would be excited. Resulting acoustic vibrations were measured with an ultrasonic microphone (*Song Meter SM4BAT FS*), positioned 1 m from the lithic (Fig. 2). Open-source audio software, *Audacity*, was used to edit the sound recordings and calculate an FFT of the vibrations recorded for each BB impact. The resulting ~ 20 spectra were averaged to increase signal-to-noise ratio and ensure that all resonant frequencies were apparent. Resonance quality factor, Q , was determined from the averaged spectra by the formula $Q = f_{\text{max}}/\text{BW}$ where f_{max} is the resonance frequency and BW the bandwidth.

In water, the resonant frequencies of the same lithics were again excited by direct percussion. Lithics sat atop a rubber band, suspended in a large cooler filled with fresh water ($\sim 0.8\text{m} \times 0.35\text{m} \times 0.3\text{m}$ interior dimensions). Each lithic was struck by a washer tied to a string, either dropped from above or jerked up from below by the experimenter. The washer hit different positions around the lithic to excite all resonance modes. Sound was recorded using the same system as before, but with an ITC-1042 hydrophone connected to the *Song Meter* recorder. Multiple spectra were obtained from the recordings and averaged as with the air measurements.

2.3. Modelling free vibration in fluids

We used the package *FinEtoolsVibInFluids.jl* (Krysl, 2017) in the *Julia* programming language (Bezanson et al., 2017) to model the natural vibrations of individual lithics in air and water. The ESNICE energy-sampling stabilized nodal-integration method based on tetrahedral meshes was employed (Sivapuram and Krysl, 2019). Lithics are

Table 1

Material properties used in the models.

	Pink Chert	Santiago Peak Metavolcanic	Obsidian	Granitic
Density, ρ [kg/m ³]	2560	2720	2360	2650
Young's Modulus, E [GPa]	91	89	70	54
Poisson's ratio, ν	0.125	0.3	0.08	0.25

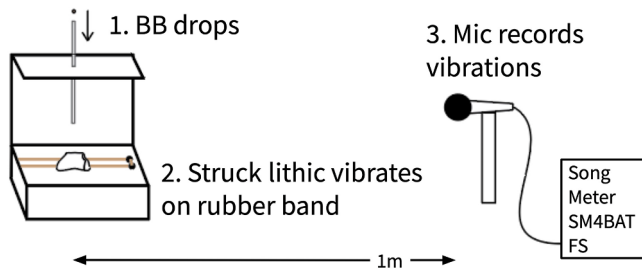


Fig. 2. Schematic for recording lithic resonance in air. Specimen rests on a rubber band and is struck by a BB dropped from above. Vibrations are recorded using an ultrasonic microphone positioned at 1 m range.

described in the model by their shape (tetrahedral mesh as in Fig. 1) and material properties (ρ, E, ν given in Table 1). The surrounding acoustic fluid is described by density ($\rho_{air} = 1.2 \text{ kg/m}^3, \rho_{water} = 1000 \text{ kg/m}^3$). From this modelling, we obtained the natural bending shapes for each lithic and the corresponding resonant frequencies (Fig. 3).

2.4. Acoustic color simulation

The acoustic color simulation uses coupled finite element and boundary element models to compute the scattered pressure field produced by an acoustic target, in this case a lithic, in a fluid medium (Fig. 4); this technique is described for axially symmetric targets in Abawi and Krysl (2017). As in the free vibration models, lithics are described by their shape (tetrahedral mesh) and material properties (ρ, E, ν (Table 1)). The surrounding acoustic fluid is here described by both density ($\rho_{air} = 1.2 \text{ kg/m}^3, \rho_{water} = 1000 \text{ kg/m}^3$) and sound speed ($c_{air} = 344 \text{ m/s}^2, c_{water} = 1500 \text{ m/s}^2$) through the medium. An acoustic source and receiver are co-located at a location specified by distance from the lithic center, r , azimuthal angle, θ , and polar angle, ϕ (measured from the lithic normal). The source emits a plane wave at a chosen frequency and the receiver records the resulting scattered pressure, providing the lithic target strength as a function of frequency and incidence angle.

2.5. Thin plate vibration approximation for lithics

The first two lithic resonance frequencies can be approximated using the free-vibrations of a thin plate. Resonance frequencies for a freely

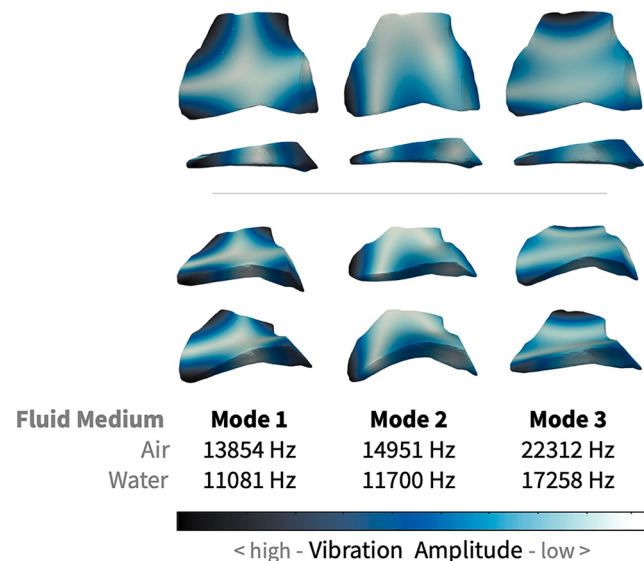


Fig. 3. Vibration bending shapes for first three modes of specimen Pink Chert 6, with corresponding resonance frequencies in air and water. Darker shading corresponds to maximum vibration amplitude, while white corresponds to displacement nulls. Both undeformed (top) and deformed (bottom) lithic shape is shown for each mode.

vibrating thin plate depend on the plate's length, width, and thickness (l, w, t) and material properties (ρ, E, ν). For plates vibrating in a fluid medium, the frequency depends on the density of the surrounding medium as well. The first two dry resonance frequencies, as well as the ratio of wet/dry frequencies, are given for pink chert and obsidian in Fig. 5. Santiago Peak metavolcanic frequencies are similar to the pink chert frequencies (within 0.5%). For a more complete treatment of vibrating plates, see Blevins (2016).

To use the thin plate approximation for lithics, we chose plate dimensions l = maximum lithic length, w = maximum lithic width, and t = average lithic thickness, where length, width, and thickness are measured along the first three principal axes of the lithics. Measurement examples are given in Fig. 6.

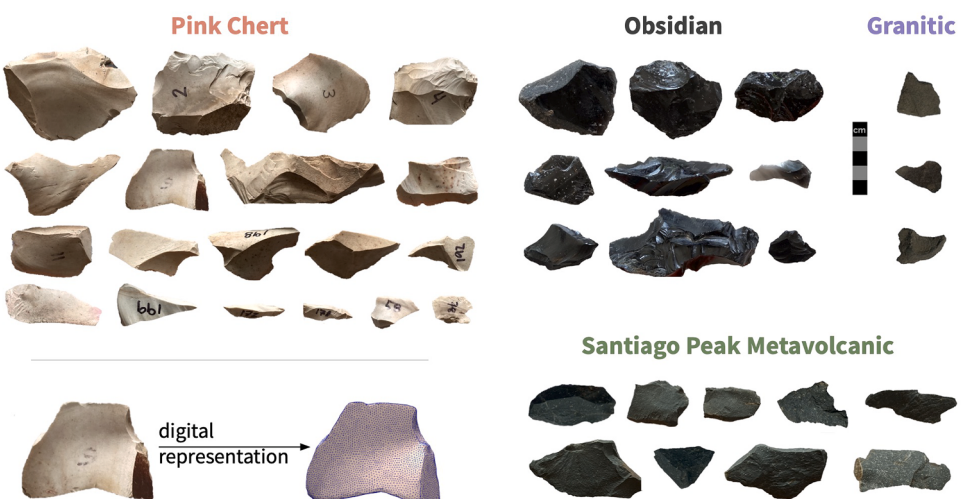


Fig. 1. Lithics used in the analysis were of four materials: obsidian ($n = 9$), pink chert ($n = 19$), Santiago Peak metavolcanic rock ($n = 9$), and granitic rock ($n = 3$). Bottom Left: Example of a typical digital representation - Pink Chert 6 is shown here. Multiple photographs were combined by photogrammetry to make a 3D mesh representation of the lithic.

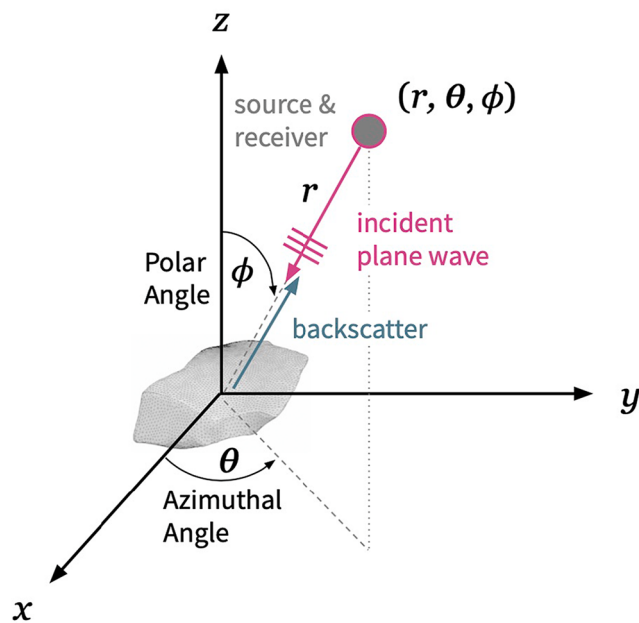


Fig. 4. Acoustic calculation geometry and coordinate system. The target lithic is positioned with its first two principal axes in the x , y plane (the Pink Chert 6 mesh is shown as an example). Co-located source/receiver location is specified by distance, r , from the lithic center, azimuthal angle, θ , and polar angle, ϕ . The source emits a plane wave at a chosen frequency, and the receiver records the backscatter.

3. Results

3.1. Measured lithic resonance in air and water

Modeled resonance frequencies for lithics freely vibrating in air were compared to measured resonance frequencies; one example for each material is shown in Fig. 7. The measured vibration spectra for each specimen show a series of distinct peaks between 5–50 kHz. The free vibration model results are overlaid as vertical lines, and the differences between modeled and measured frequencies under 50 kHz were less than 5% for all lithics, with the exception of one resonance of Granitic 4 which differed by 5.4%. The number of resonant lines and the resonant frequencies of the lines varied for each specimen, owing to the specifics of the specimen shape and material properties. This supports the validity of the model, confirming that the lithics have acoustic peaks at free vibration resonance frequencies. The in-air measured vibration spectra for the metavolcanic and granitic specimens were noticeably noisier than the other material types, with wider and shallower resonance peaks. This is reflected in the resonance quality factors which, for frequencies under 30 kHz, range from $Q \sim 100$ –670 for Pink Chert, $Q \sim 120$ –860 for Obsidian, $Q \sim 40$ –200 for Santiago Peak Metavolcanic, and $Q \sim 30$ –70 for Granitic lithics.

Modeled and measured resonance frequencies for underwater lithics are compared in Fig. 8. As with the in-air measurements, spectrum peaks occur near frequencies predicted by the free-vibration model, with the granitic lithic showing the least agreement. Some noise and erroneous lower frequencies are present due to acoustic waves bouncing around in the cooler used for measurement.

3.2. Submerged lithic acoustic response

We computed backscattered target strength from a plane wave source at a co-located receiver 5 m from the lithic. The target strength for frequencies 2–30 kHz and angles $\theta = 0$, $\phi = 0^\circ$ – 180° is shown in Fig. 9 for a single lithic, oriented as shown in Fig. 4. Strong responses appear as vertical lines in Fig. 9, at frequencies consistent with predicted

resonance frequencies. For non-resonance frequencies, maximum backscatter is observed at normal incidence ($\phi = 0^\circ$ and 180° in Fig. 9), however, at resonance frequencies the signal does not follow this pattern and maximum backscatter is typically not at normal incidence. Further, different resonant modes for the same lithic can be optimally excited at differing angles. The polar angle, ϕ_{max} , of maximum target strength is shown for every resonance of all specimens from 2–30 kHz in Fig. 10. Most resonances are maximally excited at a range of angles 42° – 66° from normal incidence. Maximum target strength appears highest at frequencies 8–16 kHz. Fig. 11 shows resonance response for polar incidence angles up to 90° averaged over the 37 modern specimens and resonance frequencies. Maximum target strength is excited at $\phi_{max} = 55^\circ$ for the average of each of the three modern-lithic materials. Averaged over these 37 lithics, over half the peak signal is excited/received between 37° – 73° from normal incidence. The average maximum target strength for the analyzed lithics is -27.83 dB, which is about 10 dB stronger than the average normal incidence response of -38.95 dB. Modelling of the three granitic lithics produced qualitatively similar results, with an average target strength of -27.45 dB at $\phi_{max} \sim 50^\circ$ and -48.33 dB at normal incidence.

4. Discussion

Lithics of varied shapes, sizes and materials have multiple resonances between 2–30 kHz in air and under water, which can be both observed by measurement and predicted by finite element free vibration models. In all cases, the lithics have visible resonance peaks in the 2–30 kHz range (examples in Fig. 7). Obsidian and chert produce distinct resonant peaks, and while the metavolcanic and granitic specimens produce noisier vibration spectra, their resonance peaks are still pronounced. This indicates that the resonance phenomenon is strong for a range of lithic materials, but the resonance quality factor, Q , decreases as the material becomes more rough and crystalline. Modelled resonance frequencies line up remarkably well with the measured spectral peaks, even for complex shapes with many resonant modes (e.g. Obsidian 13), leading to increased confidence in the model results. The coarser crystalline structure of the granitic material may decrease the model's validity for these lithics, as it approximates the lithics as homogeneous and isotropic elastic bodies. The model did, however, reasonably correspond with measured resonance frequencies, so we include model results for the granitic lithics, but keep their results separate when presenting averaged values.

Modelling of the lithics in water still results in strong resonances, with the strongest resonance response at frequencies between ~ 8 – 16 kHz (Fig. 10). These models also reveal that the maximum acoustic backscatter occurs at the resonance frequencies and is highly directional. A cross section of the results from a single lithic simulation are shown in Fig. 9. Polar angles of $\phi = 0^\circ$ and 180° correspond to the acoustic wave being normally incident on the flat face of the lithic, while $\phi = 90^\circ$ corresponds to a wave coming in from the side, directed at the sharp edge of the lithic. For most frequencies, the strongest back-scattered signals are achieved near normal incidence, which have the largest scattering cross-section, while waves incident on the sharp edge of the lithic are not strongly scattered. However, at a narrow set of frequencies, which correspond to the predicted underwater resonance frequencies, a stronger acoustic response is observed. Two important aspects of the resonant response are: (1) some resonant frequencies have a stronger signal than others, with the fundamental resonance not necessarily returning the highest amplitude; and (2) the resonance signal is strongest at angles off from the normal incidence. Excitation and reception of the resonance signal is highly directional, leading to the highest backscattered amplitude at angles $\phi_{max} = 37^\circ$ – 73° . While Fig. 9 is for a single lithic, the characteristics described are consistent for other specimens. The maximum resonance response is consistently recorded off normal incidence, regardless of lithic material or dimensions (Fig. 10). Resonance return does vary with azimuthal angle around the

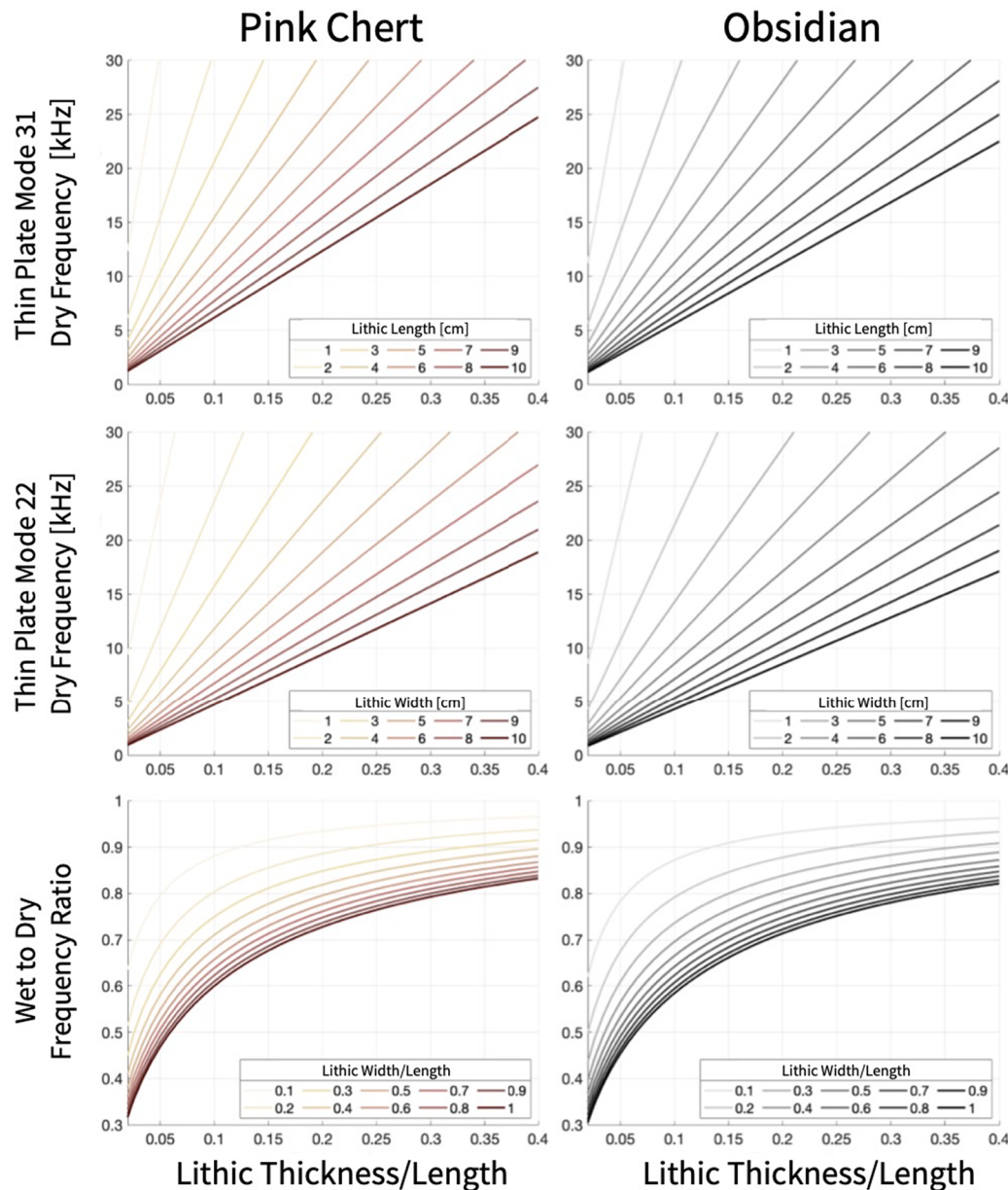


Fig. 5. Plots to estimate the first and second resonance frequencies of a thin plate freely vibrating in air and water based on its dimensions (length, width, thickness) and material (as similar to chert or obsidian). Top, Middle: Frequencies for the first and second dry resonance modes as a function of lithic dimensions. The top plot describes a mode dependent only on length and thickness, while the middle is dependent on width as well. Which frequency is lower depends on the lithic's width to length ratio, so if using this figure to estimate the fundamental frequency, we suggest estimating both and choosing the lower one. To estimate resonance frequencies, divide thickness by length and find this value on the x-axis, then go up to the line that corresponds to the plate length or width, and observe the frequency on the y-axis. Bottom: Ratio of wet/dry resonance frequencies as a function of lithic dimensions. The resonance frequencies in water will be the resonance frequencies in air multiplied by this ratio. To estimate the wet/dry ratio, divide thickness by length and find this value on the x-axis, then go up to the line that corresponds to the plate width divided by its length, and observe the ratio on the y-axis.

lithic, θ , but the pattern is individual to each lithic and θ_{\max} can even differ for different resonant modes of the same lithic. In practice, this means that, depending on the sonar path over the lithic, some resonance frequencies will be more detectable than others. Additionally, because maximum resonance is received at a consistent polar angle, lithics are likely more detectable laterally offset from the sonar instrument rather than directly below. The signal from an offset sonar path will pass through a range of azimuthal angles, increasing likelihood of hitting the lithic at its optimal angle for more frequencies.

The target strength excited at the optimal angle is significantly higher (~10 dB) than at normal incidence. On average, the maximum response is elicited at $\phi \sim 55^\circ$, likely because at these incidence angles, the acoustic wave can better align with the lithic shape in a way that excites resonance. For example, a plane wave angled off normal incidence would cause the lithic to bend into the deformed lithic resonance shapes in Fig. 3 better than would a normally incident source. The optimal polar angle is similar for all lithic materials examined. This result has practical implications, and leads to the suggestion that detection of lithics by chirped sonar may be optimized using acoustic

pulses with incidence angles $\sim 55^\circ$ toward the seabed.

This analysis focuses on individual lithics suspended in water, although lithics are not found floating in the water column and may not be alone. The next steps are to consider how burial in sediment will affect the acoustic signal and to explore the response of lithic concentrations. Burial in sediment will lower the resonance frequencies, because the sediment's density is greater than that of water. It may dampen the acoustic response, but since lithics buried up to 2 m have been detected using chirp sonar in the field (Grøn et al., 2021), burial may not be a determining factor. Substrate material may have an effect on the optimal beam angle, since the acoustic wave will change direction at the water-seafloor interface in accordance with Snell's law ($c_{water}/\sin\phi_{water} = c_{sand}/\sin\phi_{sand}$). For example, if the substrate is sand in which the speed of sound is $c_{sand} = 1650$ m/s, a 55° pulse hitting a flat water-sand interface will become 64° traveling through the sand. It may then be advisable to use a shallower beam angle to find buried lithics, so that the wave interacting with the lithics is incident near 55° .

In the case of many lithics together, we would expect to see a broad range of frequencies producing strong responses. Given enough lithics,

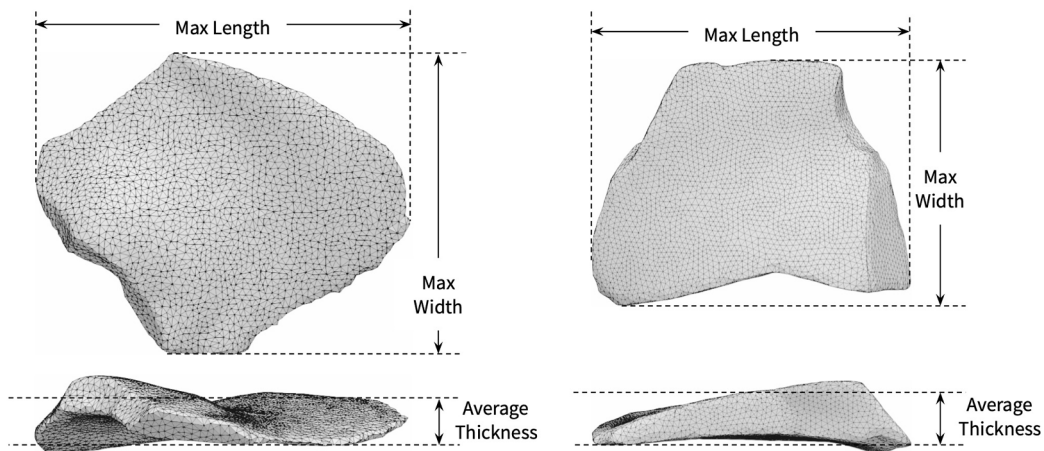


Fig. 6. Lithic dimensions used in thin plate approximation. We measured dimensions using the 3D meshes, where length, width, and thickness are measured along the first three principal axes of the lithic. We chose plate dimensions l = maximum lithic length, w = maximum lithic width, t = average lithic thickness.

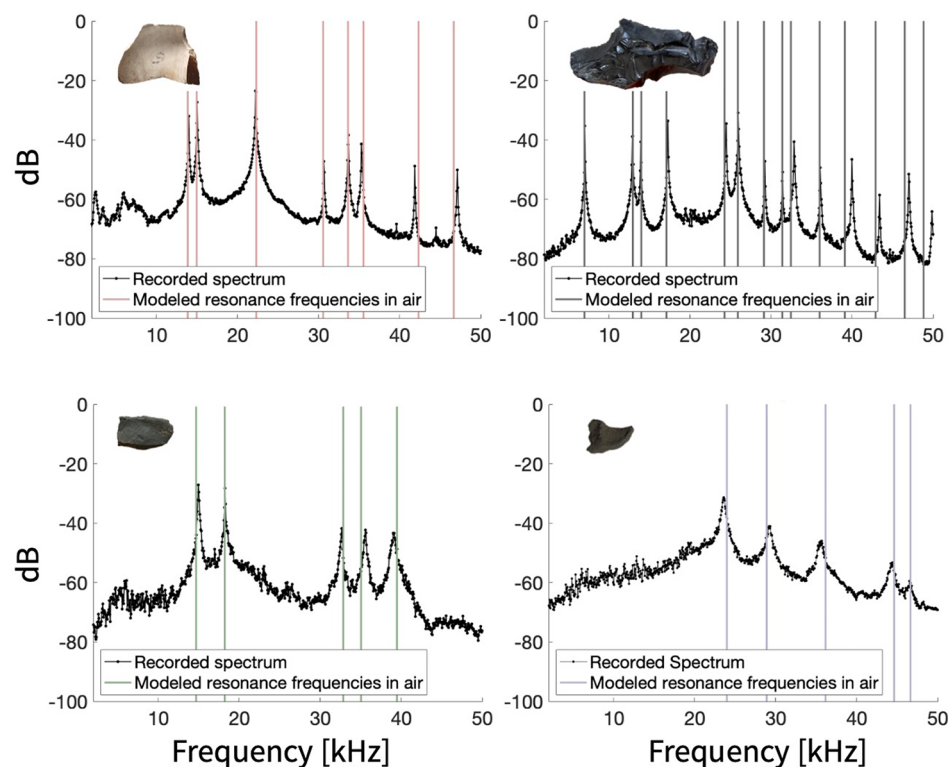


Fig. 7. Resonance spectrum measured for four lithic examples (one for each material type – Pink Chert 6, Obsidian 13, Metavolcanic 2, and Granitic 10) with free vibration model results overlaid as vertical lines. Differences between modeled and measured frequencies under 50 kHz were less than 5% for all lithics, with the exception of one resonance of the lithic named Granitic 4 which differed by 5.4%.

each with multiple resonance frequencies, the received signal may appear less like distinct, resonant peaks, and more like a consistently strong signal across many frequencies. The overall signal would depend on lithic assemblage characteristics and spatial distribution. In areas of long-term use for instance, with lithics densely deposited with depth, the lithics near the surface may shield the signal from those below. Additionally, the absence of a correlation between maximum signal and azimuthal response (θ) indicates that, even if all the lithics are aligned with their long axis in the same direction, as may be the case when lithics are re-positioned by flowing water, the maximum signal would not predictably depend on the transect path over the collection. Another way to think of this is that, for a collection of flat-laying lithics, we

expect the signature of the lithic concentration to be detectable in a cone-shaped region above the lithics whether they have random or aligned orientations. Further modelling, experiments, and field tests are needed in this area.

Our analysis shows that the first and second resonant frequencies of each lithic can be estimated using a thin plate approximation (Fig. 12), in which the plate is described by the lithic's maximum length, maximum width, average thickness (l, w, t), and material properties (E, ν, ρ). This approximation can be used to identify the expected range of resonance frequencies in archaeological contexts where there is a broad idea of what lithic dimensions and material properties should be present. For example, larger debitage could be found at areas of initial

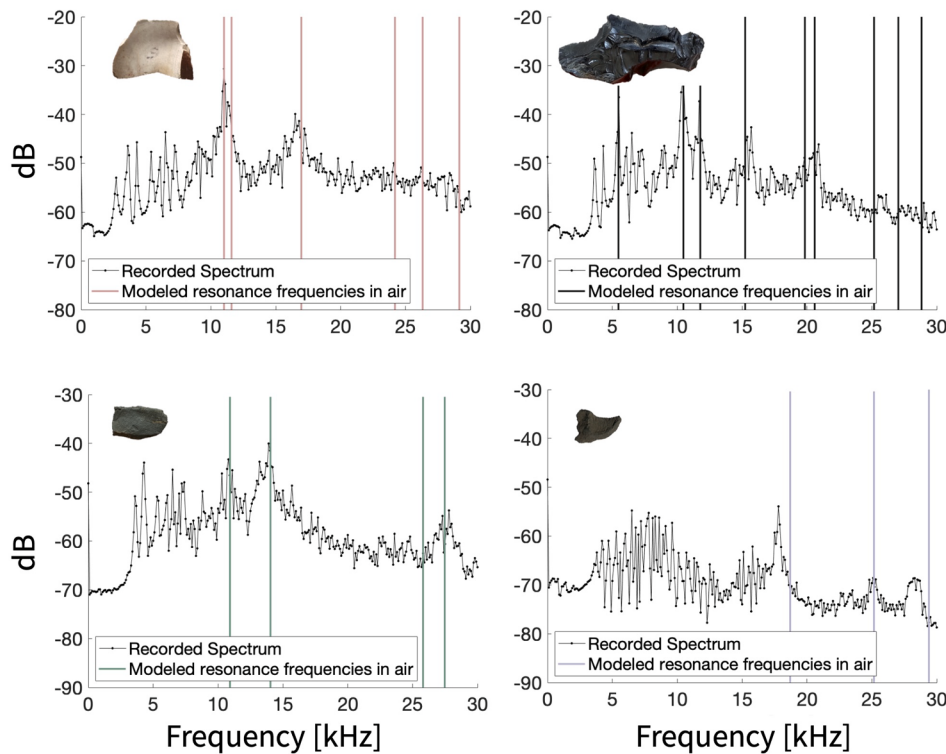


Fig. 8. Resonance spectrum measured in water for four lithic examples (one for each material type – Pink Chert 6, Obsidian 13, Metavolcanic 2, and Granitic 10) with wet free vibration model results overlaid as vertical lines. Non-modeled peaks below 10 kHz are common to all lithic spectra and are likely due to standing waves in the cooler used for measurement.

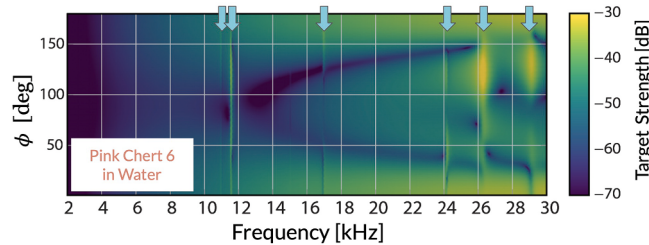


Fig. 9. Target strength plotted with respect to incident polar angle, ϕ , and frequency for the Pink Chert 6 specimen, oriented as shown in Fig. 4. Frequencies with distinctly high target strength, indicated with blue arrows, correspond to predicted free vibration frequencies in water. Color bar for target strength at right.

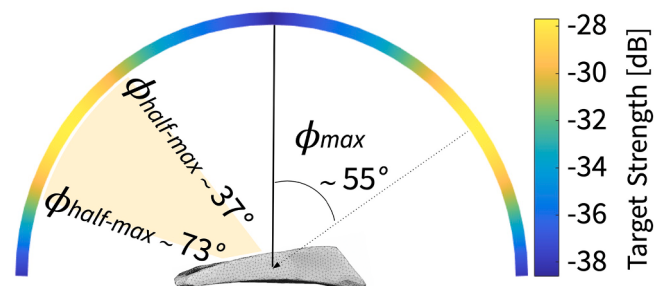


Fig. 11. Maximum target strength occurs at angles between $37^\circ - 73^\circ$ from the normal, averaged over the 37 modern specimens. The angle with maximum return is $\phi_{max} = 55^\circ$ for each material type, both separately and combined.

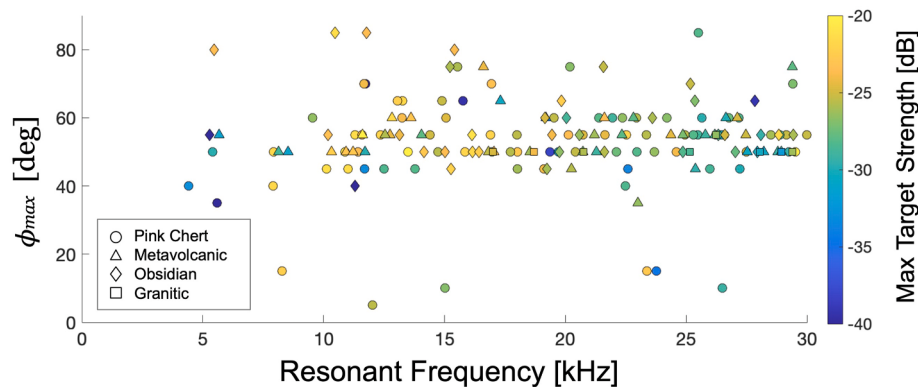


Fig. 10. Polar angle of maximum target strength, ϕ_{max} , versus resonant frequency for all modes of all specimens. ϕ_{max} is clustered around $54^\circ \pm 12^\circ$ for all materials (see symbol shape). Maximum target strength appears highest at frequencies 8–16 kHz. Color bar at right shows target strength.

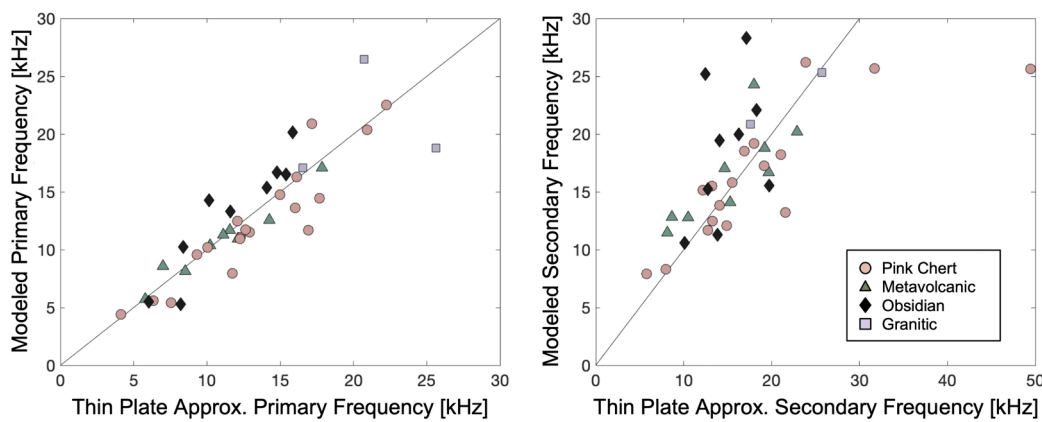


Fig. 12. Modeled lithic resonance frequencies (left primary, right secondary) in water vs. predicted resonance frequencies from a freely vibrating thin plate approximation for debitage made of pink chert (pink circles), Santiago Peak metavolcanic (green triangles), obsidian (black diamonds), and granitic rock (purple squares).

reduction or on sites of cultures with lithic traditions that include macrolithics, whereas residential or resource exploitation sites are likely to contain relatively smaller lithic tools (Joy, 2020). It may be possible to calibrate sonar parameters to focus on the expected relevant frequencies for these or other known contexts. Conversely, the thin plate approximation may be useful to gain information about lithic properties from the resonance frequencies measured in the field. As this is a rough approximation, we hope that further modelling and field work will lead to more advanced data processing methods to both detect and interpret the lithic signatures.

5. Conclusion

In this study, we simulate the acoustic response of lithic debitage in water as a step towards understanding the acoustic response of lithics in submerged sites. Strong resonance is exhibited in all lithics, with most having multiple resonances under 30 kHz. However, resonance quality appears to decrease with coarser granular structure of the lithic material, potentially making them more difficult to detect. The highest resonance signal strengths appear in the 8–16 kHz range. Models show that lithic detection based on resonance is highly directional. For flat-laying lithics, target strength at normal incidence is on average 10 dB lower than the strongest signal, found about 55° from normal incidence. We suggest that the best way to detect submerged lithics may not be through standard mono-static sub-bottom profiling with a direct downward pulse, but instead with a beam angled ~ 55° toward the sea bottom. If the lithics are buried, we suggest adjusting the beam angle so that the acoustic pulse travels through the substrate at ~ 55°.

The results presented here are for a co-located source and receiver. Since many chirp systems have a co-located source and receiver, our current results should be applicable to these existing systems. It should also be possible to design a bi-static sonar to exploit the directionality of the lithic response.

Funding

This research did not receive any specific grant from funding agencies in the public, commercial, or not-for-profit sectors. Funding for MAM provided by UCSD and the SIO Graduate Department.

CRediT authorship contribution statement

Margaret A. Morris: Methodology, Software, Validation, Formal analysis, Investigation, Data curation, Writing - original draft, Writing - review & editing, Visualization. **Petr Krysl:** Methodology, Software, Validation, Resources, Writing - review & editing, Supervision. **Isabel C.**

Rivera-Collazo: Conceptualization, Resources, Writing - review & editing, Supervision. **John A. Hildebrand:** Conceptualization, Methodology, Resources, Writing - review & editing, Supervision.

Declaration of Competing Interest

The authors declare that they have no known competing financial interests or personal relationships that could have appeared to influence the work reported in this paper.

Acknowledgements

Thanks to G. Timothy Gross for sharing debitage with us. Thanks also to Ole Grøn, for his suggestions and groundbreaking research. We thank two anonymous reviewers for their encouragement and insights which significantly improved this work.

References

- Abawi, A.T., 2017. Finite element modeling of scattering from underwater proud and buried military munitions. Strategic Environmental Research and Development Program, Alexandria, VA. Tech. rep. <https://apps.dtic.mil/sti/citations/AD1042064>.
- Abawi, A.T., Krysl, P., 2017. Coupled finite element/boundary element formulation for scattering from axially-symmetric objects in three dimensions. J. Acoust. Soc. Am. 142 (6), 3637–3648. <https://doi.org/10.1121/1.5016030>.
- Aliyu, M.M., Murphy, W., Lawrence, J.A., Collier, R., 2017. Engineering geological characterization of flints. Q. J. Eng. Geol. Hydrogeol. 50 (2), 133–147. <https://doi.org/10.1144/qjegh2015-044>.
- Astrup, P.M., Skriver, C., Benjamin, J., Stankiewicz, F., Ward, I., McCarthy, J., Ross, P., Baggaley, P., Ulm, S., Bailey, G., 2019. Underwater shell middens: excavation and remote sensing of a submerged mesolithic site at Hjarnø Denmark. J. Island Coast. Archaeol. 1–20. <https://doi.org/10.1080/15564894.2019.1584135>.
- Bailey, G.N., Flemming, N.C., 2008. Archaeology of the continental shelf: marine resources, submerged landscapes and underwater archaeology. Quatern. Sci. Rev. 27, 2153–2165. <https://doi.org/10.1016/j.quascirev.2008.08.012>.
- Bailey, G.N., King, G.C., 2011. Dynamic landscapes and human dispersal patterns: tectonics, coastlines, and the reconstruction of human habitats. Quatern. Sci. Rev. 30 (11–12), 1533–1553. <https://doi.org/10.1016/j.quascirev.2010.06.019>.
- Benjamin, J., 2010. Submerged prehistoric landscapes and underwater site discovery: Reevaluating the ‘Danish Model’ for international practice. J. Island Coastal Archaeol. 5 (2), 253–270. <https://doi.org/10.1080/15564894.2010.506623>.
- Bezanson, J., Edelman, A., Karpinski, S., Shah, V.B., 2017. Julia: a fresh approach to numerical computing. SIAM Rev. 59 (1), 65–98. <https://doi.org/10.1137/141000671>.
- Blake, E.C., Cross, I., 2008. Flint tools as portable sound-producing objects in the upper palaeolithic context: an experimental study. In: Cunningham, P., Heeb, J., Paardekooper, R. (Eds.), Experiencing Archaeology by Experiment. Oxbow Books, Oxford, pp. 1–19 tDAR id: 422095. <https://core.tdar.org/document/422095/flint-tools-as-portable-sound-producing-objects-in-the-upper-palaeolithic-context-an-experimental-study>.
- Blevins, R.D., 2016. Formulas for Dynamics, Acoustics, and Vibration. Wiley Series in Acoustics, Noise and Vibration. John Wiley & Sons, Ltd. <https://doi.org/10.1002/9781119038122>. ISBN: 9781119038115.

- Braje, T.J., Erlandson, J.M., Rick, T.C., Davis, L., Dillehay, T., Fedje, D.W., Froese, D., Gusick, A., Mackie, Q., McLaren, D., Pitblado, B., Raff, J., Reeder-Myers, L., Waters, M.R., 2019. Fladmark + 40: what have we learned about a potential pacific coast peopling of the americas? *Am. Antiq.* 85 (1), 1–21. <https://doi.org/10.1017/aq.2019.80>.
- Erlandson, J.M., 2001. The Archaeology of aquatic adaptations: Paradigms for a new millennium. *J. Archaeol. Res.* 9 (4), 287–350. <https://doi.org/10.1023/A:1013062712695>.
- European Commission, 2020. The EU Blue Economy Report 2020. Publications Office of the European Union, Luxembourg. <https://doi.org/10.2771/073370>.
- Flemming, N.C., 2020. Global experience in locating submerged prehistoric sites and their relevance to research on the american continental shelves. *J. Island Coast. Archaeol.* 1–24. <https://doi.org/10.1080/15564894.2020.1781712>.
- Flemming, N.C., Çağatay, M.N., Chiocci, F.L., Galanidou, N., Lericolais, G., Jöns, H., Missiaen, T., Moore, F., Rosentau, A., Sakellariou, D., Skar, B., Stevenson, A., Weerts, H., 2014. Land Beneath the Waves Submerged landscapes and sea level change. October 2015. Position Paper 21 of the European Marine Board, Ostend, Belgium. ISBN: 978-94-920430-3-0.
- Flemming, N.C., Harff, J., Moura, D., Burgess, A., Bailey, G.N., 2017. Introduction: Prehistoric Remains on the Continental Shelf — Why do Sites and Landscapes Survive Inundation?. John Wiley & Sons, Ltd., pp. 1–10. <https://doi.org/10.1002/9781118927823.ch1>
- Grøn, O., Boldreel, L.O., Hermand, J.P., Rasmussen, H., Dell'anno, A., Cvikel, D., Galili, E., Madsen, B., Nørmark, E., 2018. Detecting human-knapped flint with marine high-resolution reflection seismics: a preliminary study of new possibilities for subsea mapping of submerged stone age sites. *Underwater Technol.* 35 (2), 35–49. <https://doi.org/10.3723/ut.35.035>, 438.
- Grøn, O., Boldreel, L.O., Smith, M.F., Joy, S., Boumda, R.T., Mäder, A., 2021. Acoustic mapping of submerged stone age sites – a HALD approach. *MDPI Remote Sens.* 13 (3), 445. <https://doi.org/10.3390/rs13030445>.
- Grøn, O., Boldreel, L.O., Hermand, J.P., Rasmussen, H., Dell'anno, A., Cvikel, D., Galili, E., Madsen, B., Nørmark, E., 2017. Status for the development of acoustic mapping of submerged stone age sites. *IEEE/OES Acoustics in Underwater Geosciences Symposium, RIO Acoustics 2017*. <https://doi.org/10.1109/RIOAcoustics.2017.8349747>.
- Klein, C., Carmichael, R.S., 2021. Rock. Encyclopedia Britannica. <https://www.britannica.com/science/rock-geology>. (Accessed April 16, 2021).
- Hermand, J.P., Grøn, O., Asch, M., Ren, Q., 2011. Modelling flint acoustics for detection of submerged Stone Age sites. *OCEANS 2011 MTS/IEEE KONA* pp. 1–9. doi: 10.23919/OCEANS.2011.6107308. URL <https://doi.org/10.23919/OCEANS.2011.6107308>.
- Hermand, J.P., Tayong, R., 2013. Geoacoustic characterization of Stone Age cultural layers: Preliminary FE modelling. IEEE. <https://doi.org/10.1109/OCEANS-Bergen.2013.6608184>.
- Joy, S., 2020. Coastally-adapted: a developing model for coastal Paleoindian sites on the North American eastern continental shelf. *J. Island Coast. Archaeol.* 16 (1), 150–169. <https://doi.org/10.1080/15564894.2020.1803459>.
- Krysl, P., 2017. FinEtools.jl: Finite Element Tools in Julia - Github Repository (2017). URL <https://github.com/PetrKryslUCSD/FinEtoolsVibInFluids.jl>.
- Lógo, B.A., Vásárhelyi, B., 2019. Estimation of the poisson's rate of the intact rock in the function of the rigidity. *Periodica Polytechnica Civil Eng.* 63 (4), 1030–1037. <https://doi.org/10.3311/PPci.14946>.
- McCarthy, J.K., Benjamin, J., Winton, T., van Duivenvoorde, W., 2019. 3D Recording and Interpretation for Maritime Archaeology, vol. 31, 1 edn. Springer International Publishing. <https://doi.org/10.3723/ut.37.065>.
- McLaren, D., Fedje, D., Mackie, Q., Davis, L.G., Erlandson, J., Gauvreau, A., Vogelaar, C., 2020. Late Pleistocene Archaeological Discovery Models on the Pacific Coast of North America. *PaleoAmerica* 6 (1), 43–63. <https://doi.org/10.1080/2055563.2019.1670512>.
- Plets R., Dix J., Bates R., 2013. Marine Geophysics Data Acquisition, Processing and Interpretation. Guidance notes. English Heritage (April), 1–92.
- Sivapuram, R., Krysl, P., 2019. On the energy-sampling stabilization of Nodally Integrated Continuum Elements for dynamic analyses. *Finite Elem. Anal. Des.* 167, 1–53. <https://doi.org/10.1016/j.finel.2019.103322>.
- Sturt, F., Flemming, N.C., Carabias, D., Jöns, H., Adams, J., 2018. The next frontiers in research on submerged prehistoric sites and landscapes on the continental shelf. *Proc. Geol. Assoc.* 129 (5), 654–683. <https://doi.org/10.1016/j.pgeola.2018.04.008>.
- UNESCO, 2001. Official Texts of the United Nations Educational, Scientific and Cultural Organization. URL <http://www.unesco.org/new/culture/themes/underwater-cultural-heritage/2001-convention/official-text/>.
- Watts, J., Fulfrost, B., Erlandson, J., 2011. Searching for Santarosae: Surveying Submerged Landscapes for Evidence of Paleocoastal Habitation Off California's Northern Channel Islands Jack. In: B. Ford (ed.) *The Archaeology of Maritime Landscapes, When the Land Meets the Sea*, vol. 2, chap. 1, pp. 11–26. https://doi.org/10.1007/978-1-4419-8210-0_1.
- Westley, K., Quinn, R., Forsythe, W., Plets, R., Bell, T., Benetti, S., McGrath, F., Robinson, R., 2011. Mapping Submerged Landscapes Using Multibeam Bathymetric Data: A case study from the north coast of Ireland. *Int. J. Naut. Archaeol.* 40 (1), 99–112. <https://doi.org/10.1111/j.1095-9270.2010.00272.x>.